A Modified Four-Component Decomposition Method With Refined Volume Scattering Models

Yu Wang , *Student Member, IEEE*, Weidong Yu, *Member, IEEE*, Chunle Wang, and Xiuqing Liu

Abstract—In this article, a modified four-component decomposition method with refined volume scattering models is proposed for polarimetric synthetic aperture radar (SAR) image processing. In the new decomposition method, after the orientation angle compensation, the orientation angle is placed in the probability density functions. General forms of the volume scattering models and branch conditions can be obtained. Similar to the four-component scattering power decomposition with extended volume scattering model (S4R) proposed by Sato *et al.*, refined volume scattering models can be used for various land covers based on the criteria. Since the orientation angles are contained in the refined volume scattering models, the oriented buildings can be discriminated from the vegetation areas and the overestimation problem of volume scattering is substantially overcome. In this article, the performance of the proposed method is evaluated by the spaceborne C-band Gaofen-3 data and airborne L-band E-SAR data. Several approaches are employed as a comparison of the proposed methods. Experimental results show that, compared with the existing decomposition methods, the proposed method can effectively represent the scattering characteristics of the ambiguous regions, and the double-bounce scattering contributions over the urban areas can be substantially enhanced.

Index Terms—Model-based decomposition, orientation angle, polarimetric synthetic aperture radar (PolSAR), radar polarimetry, volume scattering.

I. INTRODUCTION

WITH the development of high-resolution synthetic aperture radar (SAR) image and measurement technology, SAR can be applied to many remote sensing fields. Among them, polarimetric SAR (PolSAR) plays an important role not only in civilian use but also in the military field, which can be used for building extraction, glacier inversion, disaster assessment, and so on [1]–[4].

Yu Wang and Weidong Yu are with the Department of Space Microwave Remote Sensing System, Aerospace Information Research Institute, Chinese Academy of Sciences, Beijing 100190, China, and also with the School of Electronic Information and Electrical Engineering, University of Chinese Academy of Sciences, Beijing 100039, China (e-mail: wangyu370705@163.com; ywd@mail.ie.ac.cn).

Chunle Wang and Xiuqing Liu are with the Department of Space Microwave Remote Sensing System, Aerospace Information Research Institute, Chinese Academy of Sciences, Beijing 100190, China (e-mail: clwang@mail.ie.ac.cn; lucia@mail.ie.ac.cn).

Digital Object Identifier 10.1109/JSTARS.2020.2990691

As one of the important branches of PolSAR, polarimetric target decomposition technology can be used to better understand the target scattering mechanism. Huynen's groundbreaking thesis formalized the early target decomposition theorems in PolSAR [5]–[7]. Then, some excellent publications have appeared in the literature [8]–[14], and the review of these decomposition theorems is summarized in [15]. The decomposition technique is divided into two main categories: Model-based decomposition [16]–[22] and eigenvalue-eigenvector-based decomposition [23]–[25]. Among them, the model-based decomposition is directly related to the physical scattering mechanism, which can be constructed based on coherency or covariance matrix. In the three-component decomposition method proposed by Freeman and Durden (FDD), the coherency matrix can be represented as a weighted sum of three general scattering types (surface scattering, double-bounce scattering, and volume scattering) [16]. Yamaguchi *et al.* [17], [18] added a helix scattering component based on the three-component decomposition, and the four-component decomposition methods with and without orientation angle compensation (OAC; Y4O and Y4R) were proposed to overcome the overestimation problem of volume scattering (OVS). Based on the Y4R, Sato *et al.* [20] decomposed the scattering mechanisms of various land covers with extended volume scattering model (S4R) and obtained better decomposition results. All these approaches decompose the coherency matrix using various volume scattering models, and the volume scattering model is selected based on HH-VV ratio ("magnitude balance"). There comes to a problem that not all the complete polarimetric information from the observed covariance/coherency matrix can be utilized, resulting in the OVS.

In recent decades, by improving volume scattering models and introducing auxiliary mathematical tools, many methods with improved volume scattering models [19], [26]–[30] and extended scattering components [2], [31]–[33] have been proposed to overcome the OVS and negative scattering powers. Several models were compared in benchmarking exercises to evaluate the performance of the existing decomposition methods [29], [34]. To overcome the OVS, the volume scattering models, which continuously cover all possible variations are widely used and the extended decomposition methods have been proposed [19], [22], [28], [30], [35]. Among these extended decomposition methods, the generalized volume scattering model (GVSM) proposed by Antropov *et al.* [19] is widely used to estimate the volume scattering component (FD/GVSM). Zou *et al.* [35] proposed an eigen-decomposition-based four-component decomposition method (EE4AVM). In this case, the lookup table

(LUT) is used to link eigen-decomposition method and model-based decomposition method, and the GVSM was employed to estimate the volume scattering element. Compared with the Y4O and Y4R, the method demonstrates much better performance in urban and vegetation areas. Quan *et al.* [28] proposed the extended general four-component decomposition method (ExG4URcc) by employing the GVSM and oriented dihedral scattering model. The GVSM is used to model the vegetation areas and oriented dihedral scattering model is employed to estimate the building areas. In this case, the volume scattering can be reasonably reduced. A modified general polarimetric model-based decomposition method which includes a simplified Neumann volume scattering model (SNVSM) was proposed by Xie *et al.* The volume scattering model in SNVSM is suitable for both random and nonrandom volume cases [22]. Ratha *et al.* [30] proposed a novel vegetation index for PolSAR using the GVSM to further overcome the OVS. Although the improved volume scattering models have been demonstrated to be effective for the inevitable defects (OVS and negative scattering powers) and these improved models substantially enhance the decomposition performance, the methods are limited by the computational efficiency due to the additional parameters. When the rotation angle between the vertical wall of the oriented building and the flight direction is small, the OAC can be used to effectively reduce the cross-pol power by minimizing the term T_{33} in the coherency matrix. However, when the rotation angle between the vertical wall of the oriented building and the direction of flight exceeds a specified range, the OAC is no longer effective, and the oriented building induces a strong cross-pol power contribution [36], [37]. The non-negative eigenvalue decomposition method selects the optimal coefficients by designing the semipositive residual coherency matrix and yields the optimal decomposition result [21], [38]. However, the computational complexity of the optimal coefficients limits the calculation load, and, therefore, the effectiveness of the method should be further evaluated.

Theoretically, the coherency matrix should be completely deoriented to avoid the scattering mechanism ambiguity. However, the orientation angle cannot be completely used in the coherency matrix and the OAC is no longer valid, which leads to the OVS. According to the inevitable shortcomings of OAC, to minimize the influence of target orientation on the coherency matrix, a modified four-component decomposition method (ExS4R) is proposed in this article. In the ExS4R, the full deorientation could be applied to the coherency matrix by placing the orientation angles in the probability density functions, and these modified probability density functions minimize the HV scattering component of the coherency matrix. The refined volume scattering models are proposed and the model to be used is determined using the HH-VV ratio ("magnitude balance"). By selecting various volume scattering models, the scattering characteristics of various terrain types with different orientation angles can be reasonably characterized to avoid ambiguity of the scattering mechanism. Different from traditional model-based decomposition (FDD, Y4R, S4R, etc.), the proposed method utilizes all the complete polarimetric information from the

observed coherency matrix. Since the proposed algorithm does not require branch parameters and optimal parameters obtained through loop iterations, it is not limited by the computational efficiency.

The performance of the proposed method is evaluated experimentally on the spaceborne C-band Gaofen-3 (GF-3) data acquired over San Francisco area in USA and the airborne L-band E-SAR data over Oberpfaffenhofen area in Germany. The FDD, FD/GVSM, Y4R, S4R, ExG4URcc, SNVSM, and EE4AVM are employed to compare with the ExS4R. The advantages of the proposed method are demonstrated in terms of the ability to decompose the scattering mechanisms of various land covers, the ability to reduce the percentage of negative scattering powers, and the calculation load.

II. METHODOLOGY

For PolSAR, the full polarimetric information can be expressed in the form of the scattering matrix, which is defined as follows:

$$[S] = \begin{bmatrix} S_{HH} & S_{HV} \\ S_{VH} & S_{VV} \end{bmatrix} = \begin{bmatrix} a & c \\ c & b \end{bmatrix} \tag{1}$$

where $S_{HV} = S_{VH} = c$, which is consistent with the reciprocity assumption. Since the term S_{HV} cannot be neglected, the scattering matrix rotated by the angle θ_d around the radar line of sight is expressed as follows:

$$[S'] = R_2(\theta_d) \begin{bmatrix} S_{HH} & S_{HV} \\ S_{VH} & S_{VV} \end{bmatrix} R_2(\theta_d)^H \tag{2}$$

where "^{H}" denotes the complex conjugate transpose. The rotation matrix of the polarization basis transformation is

$$R_2(\theta_d) = \begin{bmatrix} \cos\theta_d & \sin\theta_d \\ -\sin\theta_d & \cos\theta_d \end{bmatrix}. \tag{3}$$

For the case of monostatic backscattering, independent and identically distributed samples are averaged to form the coherency matrix, which can be expressed as follows:

$$\langle[T]\rangle = \begin{bmatrix} T_{11} & T_{12} & T_{13} \\ T_{21} & T_{22} & T_{23} \\ T_{31} & T_{32} & T_{33} \end{bmatrix} = \frac{1}{N} \sum_N k \cdot k^H \tag{4}$$

where k represents the Pauli scattering vector and N denotes the number of multi-look.

The coherency matrix rotated by the OAC is

$$\langle[T']\rangle = [R(\theta_d)] \langle[T]\rangle [R(\theta_d)]^H \tag{5}$$

where the rotation matrix of the coherency matrix is

$$[R(\theta_d)] = \begin{bmatrix} 1 & 0 & 0 \\ 0 & \cos 2\theta_d & \sin 2\theta_d \\ 0 & -\sin 2\theta_d & \cos 2\theta_d \end{bmatrix}. \tag{6}$$

The rotation angle θ_d, which minimizes the term T_{33}, is defined as follows:

$$\theta_d = \frac{1}{4}\tan^{-1}\left(\frac{2\mathrm{Re}\,(T_{23})}{T_{22} - T_{33}} \pm n\pi\right), n = 0, 1. \quad (7)$$

The mathematical forms of the coherency matrix elements are derived as follows [17]:

$$T'_{11} = (G_1 + G_3 + G_3^* + G_6)/2$$
$$T'_{12} = (G_1 - G_3 + G_3^* - G_6)/2$$
$$T'_{13} = G_2 + G_5^*$$
$$T'_{22} = (G_1 - G_3 - G_3^* + G_6)/2$$
$$T'_{23} = G_2 - G_5^*$$
$$T'_{33} = G_4 \quad (8)$$

where

$$G_1 = |a|^2 I_1 + |b|^2 I_2 + |c|^2 I_3 + 2\mathrm{Re}\,(ab^*)\,I_4$$
$$+ 2\mathrm{Re}\,(ac^*)\,I_5 + 2\mathrm{Re}\,(bc^*)\,I_6$$

$$G_2 = a\frac{b^* - a^*}{2}I_5 + b\frac{b^* - a^*}{2}I_6 + c\frac{b^* - a^*}{2}I_3$$
$$+ ac^* I_{10} + bc^* I_9 + |c|^2 I_8$$

$$G_3 = \left(|a|^2 + |b|^2\right)I_4 - |c|^2 I_3 + ab^* I_1 + a^* b I_2$$
$$+ (b^* c - ac^*)\,I_5 + (a^* c - bc^*)\,I_6$$

$$G_4 = |a|^2 I_2 + |b|^2 I_1 + |c|^2 I_3 + 2\mathrm{Re}\,(ab^*)\,I_4$$
$$- 2\mathrm{Re}\,(ac^*)\,I_6 - 2\mathrm{Re}\,(bc^*)\,I_5$$

$$G_5 = a^*\frac{b - a}{2}I_6 + b^*\frac{b - a}{2}I_5 - c^*\frac{b - a}{2}I_3$$
$$+ ca^* I_9 + b^* c I_{10} - |c|^2 I_8$$

$$G_6 = \frac{1}{4}|b - a|^2 I_3 + |c|^2 I_7 + \mathrm{Re}\left\{c^*\,(b - a)\right\}I_8 \quad (9)$$

and

$$I_1 = \int_0^{2\pi} \cos^4\theta\, p\,(\theta)\,d\theta, I_2 = \int_0^{2\pi} \sin^4\theta\, p\,(\theta)\,d\theta$$

$$I_3 = \int_0^{2\pi} \sin^2 2\theta\, p\,(\theta)\,d\theta, I_4 = \int_0^{2\pi} \sin^2\theta\cos^2\theta\, p\,(\theta)\,d\theta$$

$$I_5 = \int_0^{2\pi} \cos^2\theta \sin 2\theta\, p\,(\theta)\,d\theta, I_6 = \int_0^{2\pi} \sin^2\theta \sin 2\theta\, p\,(\theta)\,d\theta$$

$$I_7 = \int_0^{2\pi} \cos^2 2\theta\, p\,(\theta)\,d\theta, I_8 = \int_0^{2\pi} \sin 2\theta \cos 2\theta\, p\,(\theta)\,d\theta$$

$$I_9 = \int_0^{2\pi} \sin^2\theta \cos 2\theta\, p\,(\theta)\,d\theta, I_{10} = \int_0^{2\pi} \cos^2\theta \cos 2\theta\, p\,(\theta)\,d\theta \quad (10)$$

where $p(\theta)$ is the probability density function of the coherency matrix.

After the OAC, T_{33} term of the coherency matrix is minimized and the rotated coherency matrix can be decomposed into the weighted sum of four scattering components, including surface, volume, double-bounce, and helix scattering components [18], [20].

$$\langle[T']\rangle = f_s\langle[T]\rangle_s + f_d\langle[T]\rangle_d + f_c\langle[T]\rangle_c + f_v\langle[T]\rangle_v$$

$$= f_s\begin{bmatrix} 1 & \beta^* & 0 \\ \beta & |\beta|^2 & 0 \\ 0 & 0 & 0 \end{bmatrix} + f_d\begin{bmatrix} |\alpha|^2 & \alpha & 0 \\ \alpha^* & 1 & 0 \\ 0 & 0 & 0 \end{bmatrix}$$

$$+ f_c\begin{bmatrix} 0 & 0 & 0 \\ 0 & 1 & \pm j \\ 0 & \mp j & 1 \end{bmatrix} + f_v\langle[T]\rangle_v \quad (11)$$

where f_s, f_d, f_c, and f_v are coefficiencies to be determined. $\langle[T]\rangle_s$, $\langle[T]\rangle_d$, $\langle[T]\rangle_c$, and $\langle[T]\rangle_v$ are the models corresponding to surface, double-bounce, helix, and volume scattering, respectively. Surface scattering, double-bounce scattering, and helix scattering models are identical to the traditional four-component decomposition method, and the expressions of the volume scattering models used herein are introduced in the next section.

A. Four-Component Decomposition With Refined Volume Scattering Model

In the S4R, according to the generation of the cross-pol HV term, four volume-scattering models in [20] are divided into the following two parts: The volume scattering generated by the vegetation and the volume scattering generated by the oriented dihedral scattering. Among them, for the volume scattering component generated by vegetation, according to the ratio of $|S_{\mathrm{HH}}|^2$ to $|S_{\mathrm{VV}}|^2$, one of the following distributions is selected [17], [20]: (1) Sinusoidal distribution; (2) cosine distribution; (3) uniform scattering.

1) Sinusoidal distribution: $p(\theta) = \frac{1}{2}\sin(\theta - \theta_d)$, for $\theta_d < \theta < \pi + \theta_d$, with $\int_{\theta_d}^{\pi+\theta_d} p(\theta)d\theta = 1$.

The angle θ in the distribution is taken from the horizontal axis seen from the radar and θ_d denotes the orientation angle.

In this case, the integrals defined in (10) are obtained as follows:

$$I_1 = \frac{3}{8} - \frac{1}{6}\cos 2\theta_d - \frac{1}{120}\cos 4\theta_d, I_3 = \frac{1}{2} + \frac{1}{30}\cos 4\theta_d$$

$$I_2 = \frac{3}{8} + \frac{1}{6}\cos 2\theta_d - \frac{1}{120}\cos 4\theta_d, I_4 = \frac{1}{8} + \frac{1}{120}\cos 4\theta_d$$

$$I_5 = \frac{1}{3}\sin 2\theta_d + \frac{1}{15}\sin 4\theta_d, I_6 = \frac{1}{3}\sin 2\theta_d - \frac{1}{15}\sin 4\theta_d$$

$$I_9 = -\frac{1}{4} - \frac{1}{6}\cos 2\theta_d + \frac{1}{60}\cos 4\theta_d, I_8 = \frac{2}{15}\sin 4\theta_d$$

$$I_7 = \frac{1}{2} - \frac{1}{30}\cos 4\theta_d, I_{10} = \frac{1}{4} - \frac{1}{6}\cos 2\theta_d - \frac{1}{60}\cos 4\theta_d. \quad (12)$$

When the sinusoidal distribution is selected, the volume scattering model is equal to a cloud of randomly oriented, very thin horizontal cylinder-like scatterers (the vertical dipole). The

volume scattering averaged coherency matrix $\langle[T]\rangle_v$ can be written as follows:

$$\langle[T]\rangle_v = \begin{bmatrix} \frac{1}{2} & \frac{\cos 2\theta_d}{6} & \frac{\sin 2\theta_d}{3} \\ \frac{\cos 2\theta_d}{6} & \frac{15-\cos 4\theta_d}{60} & -\frac{\sin 4\theta_d}{15} \\ \frac{\sin 2\theta_d}{3} & -\frac{\sin 4\theta_d}{15} & \frac{15+\cos 4\theta_d}{60} \end{bmatrix}. \quad (13)$$

The element relations can be written as follows:

$$T'_{11} = f_s + f_d|\alpha|^2 + 1/2f_v$$

$$T'_{22} = f_s|\beta|^2 + f_d + (1/4 - \cos 4\theta_d/60)\, f_v + 1/2f_c$$

$$T'_{12} = f_s\beta^* + f_d\alpha + f_v\cos 2\theta_d/6$$

$$\mathrm{Im}(T'_{23}) = \pm f_c/2$$

$$T'_{33} = (1/4 + \cos 4\theta_d/60)\, f_v + 1/2f_c. \quad (14)$$

According to the above relations, the elements f_v and f_c can be derived directly and a set of three equations are provided to obtain remaining four unknowns (α, β, f_s, and f_d). The coefficients and their relationships can be expressed as follows:

$$f_c = 2\,|\mathrm{Im}(T_{23})|$$

$$f_v = (60T'_{33} - 30f_c)/(15 + \cos 4\theta_d)$$

$$S = f_s + f_d|\alpha|^2 = T'_{11} - 1/2f_v$$

$$C = f_s\beta^* + f_d\alpha = T'_{12} - f_v\cos 2\theta_d/6$$

$$D = f_s|\beta|^2 + f_d = T'_{22} - f_c/2 - (15 - \cos 4\theta_d)\, f_v/60. \quad (15)$$

2) Cosine distribution: $p(\theta) = \frac{1}{2}\cos(\theta - \theta_d)$, for $\theta_d < \theta < \pi + \theta_d$, with $\int_{\theta_d}^{\pi+\theta_d} p(\theta)d\theta = 1$.

Similar to the sinusoidal contribution, the elements of the volume scattering model have similar representations. When the cosine distribution is selected, the volume scattering model is equal to a cloud of randomly oriented, very thin vertical cylinder-like scatterers (the horizontal dipole), and the volume scattering averaged coherency matrix $\langle[T]\rangle_v$ can be written as follows:

$$\langle[T]\rangle_v = \begin{bmatrix} \frac{1}{2} & -\frac{\cos 2\theta_d}{6} & -\frac{\sin 2\theta_d}{3} \\ -\frac{\cos 2\theta_d}{6} & \frac{15-\cos 4\theta_d}{60} & -\frac{\sin 4\theta_d}{15} \\ -\frac{\sin 2\theta_d}{3} & -\frac{\sin 4\theta_d}{15} & \frac{15+\cos 4\theta_d}{60} \end{bmatrix}. \quad (16)$$

Similar to (14), after the expansion and rearrangement, the coefficients and their relationships can be expressed as follows:

$$f_c = 2\,|\mathrm{Im}(T_{23})|$$

$$f_v = (60T'_{33} - 30f_c)/(15 + \cos 4\theta_d)$$

$$S = f_s + f_d|\alpha|^2 = T'_{11} - f_v/2$$

$$C = f_s\beta^* + f_d\alpha = T'_{12} + f_v\cos 2\theta_d/6$$

$$D = f_s|\beta|^2 + f_d = T'_{22} - f_c/2 - (15 - \cos 4\theta_d)\, f_v/60. \quad (17)$$

3) Uniform distribution: $p(\theta) = \frac{1}{2\pi}$.

In this case, similar to the Y4R, the coherency matrix $\langle[T]\rangle_v$ can be written as follows:

$$\langle[T]\rangle_v = \frac{1}{4}\begin{bmatrix} 2 & 0 & 0 \\ 0 & 1 & 0 \\ 0 & 0 & 1 \end{bmatrix}. \quad (18)$$

After a similar expansion and rearrangement of (14), a similar set of three equations with four unknowns can be obtained

$$f_c = 2\,|\mathrm{Im}(T_{23})|\,, f_v = 4T'_{33} - 2f_c$$

$$S = f_s + f_d|\alpha|^2 = T'_{11} - f_v/2$$

$$D = f_s|\beta|^2 + f_d = T'_{22} - T'_{33}$$

$$C = f_s\beta^* + f_d\alpha = T'_{12}. \quad (19)$$

4) Volume scattering caused by oriented dihedral scatter: $p(\theta) = \frac{1}{2}\cos(\theta - \theta_d)$, for $\theta_d < \theta < \pi + \theta_d$, with $\int_{\theta_d}^{\pi+\theta_d} p(\theta)d\theta = 1$.

The HV term generated by the oriented building is different from the HV term generated by the vegetation. Therefore, the performance in distinguishing between buildings and vegetation areas is unacceptable with a uniform volume scattering model. In addition, the cross-pol power generated by the oriented building is different from the double-bounce scattering power. Therefore, the scattering components in urban areas cannot be fully represented by the double-bounce scattering model. Based on the coherency matrix of rotated dihedral elementary scatterers with an orientation angle of θ_d, namely, $T_d(\theta_d)$, and the refined probability density function, the coherency matrix elements of volume scattering can be obtained.

The scattering matrix of the oriented building can be depicted as follows:

$$T_d(\theta_d) = \begin{bmatrix} 0 & 0 & 0 \\ 0 & \cos^2 2\theta_d & 0 \\ 0 & 0 & \sin^2 2\theta_d \end{bmatrix}. \quad (20)$$

According to the integral relationship between the probability density function and the coherency matrix, the theoretical ensemble matrix for oriented building reflection can be derived as follows:

$$\langle[T]\rangle_v = \int_{\theta_d}^{\pi+\theta_d} T_d(\theta_d)\, p(\theta)\, d\theta. \quad (21)$$

The coherency matrix $\langle[T]\rangle_v$ can be written as follows:

$$\langle[T]\rangle_v = \begin{bmatrix} 0 & 0 & 0 \\ 0 & \frac{15-\cos 4\theta_d}{30} & 0 \\ 0 & 0 & \frac{15+\cos 4\theta_d}{30} \end{bmatrix}. \quad (22)$$

After the rearrangement, the coefficients and their relationships can be expressed as follows:

$$f_c = 2\,|\mathrm{Im}(T_{23})|$$

$$f_v = (30T'_{33} - 15f_c)/(15 + \cos 4\theta_d)$$

$$S = f_s + f_d|\alpha|^2 = T'_{11}$$

$$C = f_s\beta^* + f_d\alpha = T'_{12}$$

$$D = f_s|\beta|^2 + f_d = T'_{22} - f_c/2 - (15 - \cos 4\theta_d)\, f_v/30. \quad (23)$$

From the volume scattering models obtained by the above new probability distributions, it can be seen that when $\theta_d = 0$, the previously described volume scattering models are the same as the volume scattering models in the S4R. Moreover, when $\theta_d \neq 0$, the volume scattering models are related to the orientation angles and can be used to characterize the volume scattering components with various orientation angles. These volume scattering models are used to effectively describe the volume scattering powers of targets with various orientation angles and to overcome the OVS.

B. Solution of Undetermined Equation

It is necessary to solve (15), (17), (19), and (23) by making assumptions in advance in order to reduce the number of unknowns. After the subtraction of the volume scattering and helix scattering components, the dominant scattering mechanism (the double-bounce scattering or the surface scattering) of the residual matrix depends on the value of $\mathrm{Re}\{\langle S_{\mathrm{HH}}S_{\mathrm{VV}}^*\rangle\}$ [16]. The non-dihedral scattering of vegetation makes $\mathrm{Re}\{\langle S_{\mathrm{HH}}S_{\mathrm{VV}}^*\rangle\}$ positive, whereas the dihedral scattering of oriented buildings makes $\mathrm{Re}\{\langle S_{\mathrm{HH}}S_{\mathrm{VV}}^*\rangle\}$ negative. In the proposed method, the dominant scattering can be discriminated by the derivation result of $\mathrm{Re}\{\langle S_{\mathrm{HH}}S_{\mathrm{VV}}^*\rangle\}$, which is expressed as follows:

$$\mathrm{Re}\left\{f_s\beta + f_d\alpha^*\right\} + f_v/8 - f_c/4 = \mathrm{Re}\left\{\langle S_{\mathrm{HH}}S_{\mathrm{VV}}^*\rangle\right\}. \quad (24)$$

The branch condition can be rearranged as follows:

$$\begin{aligned} C_1 &= 2\mathrm{Re}\left\{f_s\beta + f_d\alpha^*\right\} \\ &= 2\mathrm{Re}\left\{\langle S_{\mathrm{HH}}S_{\mathrm{VV}}^*\rangle\right\} - f_v/4 + f_c/2 \\ &= T'_{11} - T'_{22} - T'_{33} + f_c = 2T_{11} - \mathrm{Span} + f_c \end{aligned} \quad (25)$$

where Span is the total backscattering power of the scattering mechanisms.

If $C_1 > 0$, surface scattering is the dominant mechanism. Since the double-bounce component is negligible, the value of α is approximately 0 and can be assumed to be equal to 0. In this condition, the solutions of the undetermined equations are as follows:

$$f_s = S, \beta^* = \frac{C}{S}, f_d = D - \frac{|C|^2}{S}. \quad (26)$$

If $C_1 \leq 0$, double-bounce scattering is the dominant mechanism. Since the surface component is negligible, the value of $|\beta|$ is approximately 0 and can be assumed to be equal to 0. In this condition, the solutions of the undetermined equations are as follows:

$$f_d = D, \alpha = \frac{C}{D}, f_s = S - \frac{|C|^2}{D}. \quad (27)$$

Once these coefficients are determined, the scattering powers can be expressed as follows:

$$\begin{aligned} P_s &= f_s\left(1 + |\beta|^2\right) \\ P_d &= f_d\left(1 + |\alpha|^2\right) \\ P_v &= f_v, P_c = f_c. \end{aligned} \quad (28)$$

In addition, the scattering powers are equally applicable to the oriented dihedral scattering areas.

C. Decomposition Algorithm Implementation

In the S4R, the oriented dihedral scattering model is very suitable for building areas with large orientation angles, while for building areas with small orientation angles, one of the volume scattering models of the vegetation area is selected, which may result in the OVS. In the method proposed in this article, the refined volume scattering models containing the orientation angles of various landscapes are used to represent the volume scattering mechanisms. For buildings with various orientation angles to the direction of the radar line of sight, reasonable characterization can be performed to obtain better decomposition results. In the decomposition process of the proposed method, the calculation of the helix scattering power is directly performed. Then, a branch condition is used to distinguish whether the HV component is generated by the oriented building area or the vegetation area. Similar to (24), the decision threshold can be written as follows:

$$\begin{aligned} &\mathrm{Re}\left\{\langle S_{\mathrm{HH}}S_{\mathrm{VV}}^*\rangle\right\} \\ &\quad = \mathrm{Re}\left\{f_s\beta + f_d\alpha^*\right\} - (15 - \cos 4\theta_d)\,f_v/60 - f_c/4 \\ &C_0 = 2\mathrm{Re}\left\{f_s\beta + f_d\alpha^*\right\} \\ &\quad = 2\mathrm{Re}\left\{\langle S_{\mathrm{HH}}S_{\mathrm{VV}}^*\rangle\right\} + (15 - \cos 4\theta_d)\,f_v/30 + f_c/2 \\ &\quad = T'_{11} + T'_{22} + \frac{15 - \cos 4\theta_d}{15 + \cos 4\theta_d}T'_{33} + \frac{\cos 4\theta_d}{15 + \cos 4\theta_d}f_c. \end{aligned} \quad (29)$$

It can be seen from (29) that when $\theta_d = 0$, the branch condition is consistent with the S4R; when $\theta_d \neq 0$, the branch condition is related to the orientation angle, and various landscapes with various orientation angles can be reasonably characterized.

When $C_0 > 0$, one of the refined vegetation scattering models is selected to obtain the volume scattering power of the target, and the principle of the selection depends on the magnitude balance of $|S_{\mathrm{HH}}|^2$ and $|S_{\mathrm{VV}}|^2$. When $C_0 \leq 0$, the volume scattering caused by oriented dihedral scatterer is selected. After selecting the appropriate volume scattering model, the dominant scattering mechanism (double-bounce scattering or surface scattering) of the residual matrix is determined according to the aforementioned branch condition C_1. This new decomposition method accounts for inclusion of all the elements of the coherency matrix. The method implementation flowchart is shown in Fig. 1.

III. RESULTS AND DISCUSSIONS

A. Discussion of the Decomposition Results

To evaluate the performance of the proposed decomposition method, spaceborne C-band GF-3 data located in San Francisco, USA, is selected as the study site and the image includes buildings with various orientation angles, roads, forests, and oceans. The data was collected on September 15, 2017 and the acquisition mode is ascending. The corresponding incidence angle range varies from $19.86°$ to $22.59°$ and the central coordinates are $(37.6°\mathrm{N}, 122.4°\mathrm{W})$. The azimuth and range resolutions of the image correspond to 8×8 m and the multi-look number is 9×9 (azimuth $\times$ range). A refined Lee filter has been applied to smooth the speckle effect using a 7×7 moving window. An

Rotated coherency matrix

$$\langle[T']\rangle = [R(\theta_d)] \begin{bmatrix} T_{11} & T_{12} & T_{13} \\ T_{21} & T_{22} & T_{23} \\ T_{31} & T_{32} & T_{33} \end{bmatrix} [R(\theta_d)]^{\mathrm{H}} \quad [R(\theta_d)] = \begin{bmatrix} 1 & 0 & 0 \\ 0 & \cos 2\theta_d & \sin 2\theta_d \\ 0 & -\sin 2\theta_d & \cos 2\theta_d \end{bmatrix}$$

$$\theta_d = \frac{1}{4}\tan^{-1}\left(\frac{2\operatorname{Re}(T_{23})}{T_{22} - T_{33}}\right)$$

Four-component decomposition

$$P_c = 2|\operatorname{Im}(T'_{23})|$$

$$C_0 = T'_{11} + T'_{22} + \frac{15 - \cos 4\theta_d}{15 + \cos 4\theta_d}T'_{33} + \frac{\cos 4\theta_d}{15 + \cos 4\theta_d}P_c$$

Surface scattering

$C_0 > 0$

Yes   No   Double-bounce scattering

Volume Scattering power

$$10\log\left[\frac{T'_{11} + T'_{22} - 2\operatorname{Re}(T'_{12})}{T'_{11} + T'_{22} + 2\operatorname{Re}(T'_{12})}\right]$$

-2 dB   2 dB

$$P_v = \frac{60T'_{33} - 30f_c}{15 + \cos 4\theta_d}$$

$$P_v = 4T'_{33} - 2P_c$$

$$P_v = \frac{60T'_{33} - 30f_c}{15 + \cos 4\theta_d}$$

$$P_v = \frac{30T'_{33} - 15P_c}{15 + \cos 4\theta_d}$$

If $P_v < 0$, then $P_c = 0$. ⟹ Three component decomposition (P_s, P_d, P_v)

$$S = T'_{11} - 1/2P_v$$
$$D = T'_{22} - \frac{P_c}{2} - \frac{P_v(15 - \cos 4\theta_d)}{60}$$
$$C = T'_{12} - P_v\cos 2\theta_d/6$$

$$S = T'_{11} - 1/2P_v$$
$$D = T'_{22} - T'_{33}$$
$$C = T'_{12}$$

$$S = T'_{11} - 1/2P_v$$
$$D = T'_{22} - \frac{P_c}{2} - \frac{P_v(15 - \cos 4\theta_d)}{60}$$
$$C = T'_{12} + P_v\cos 2\theta_d/6$$

$$S = T'_{11}$$
$$D = T'_{22} - \frac{P_c}{2} - \frac{(15 - \cos 4\theta_d)}{30}P_v$$
$$C = T'_{12}$$

$$Span = T_{11} + T_{22} + T_{33}$$

$P_s = P_d = 0$ Yes $P_v + P_c > Span$ No

$$C_1 = 2T_{11} - Span + P_c$$

Surface scattering   Yes $C_1 > 0$ No   Double-bounce scattering

$$P_s = S + |C|^2/S$$
$$P_d = D - |C|^2/S$$

$$P_s = S - |C|^2/D$$
$$P_d = D + |C|^2/D$$

If $P_s > 0 \quad P_d > 0$ $P_s > 0 \quad P_d < 0$ $P_s < 0 \quad P_d > 0$

$$P_d = P_s = 0$$
$$P_c, P_v = Span - P_c$$

$$P_d, P_s, P_c, P_v$$
$$Span = P_d + P_s + P_v + P_c$$

$$P_c, P_v, P_d = 0$$
$$P_s = Span - P_c - P_v$$

$$P_c, P_v, P_s = 0$$
$$P_d = Span - P_c - P_v$$

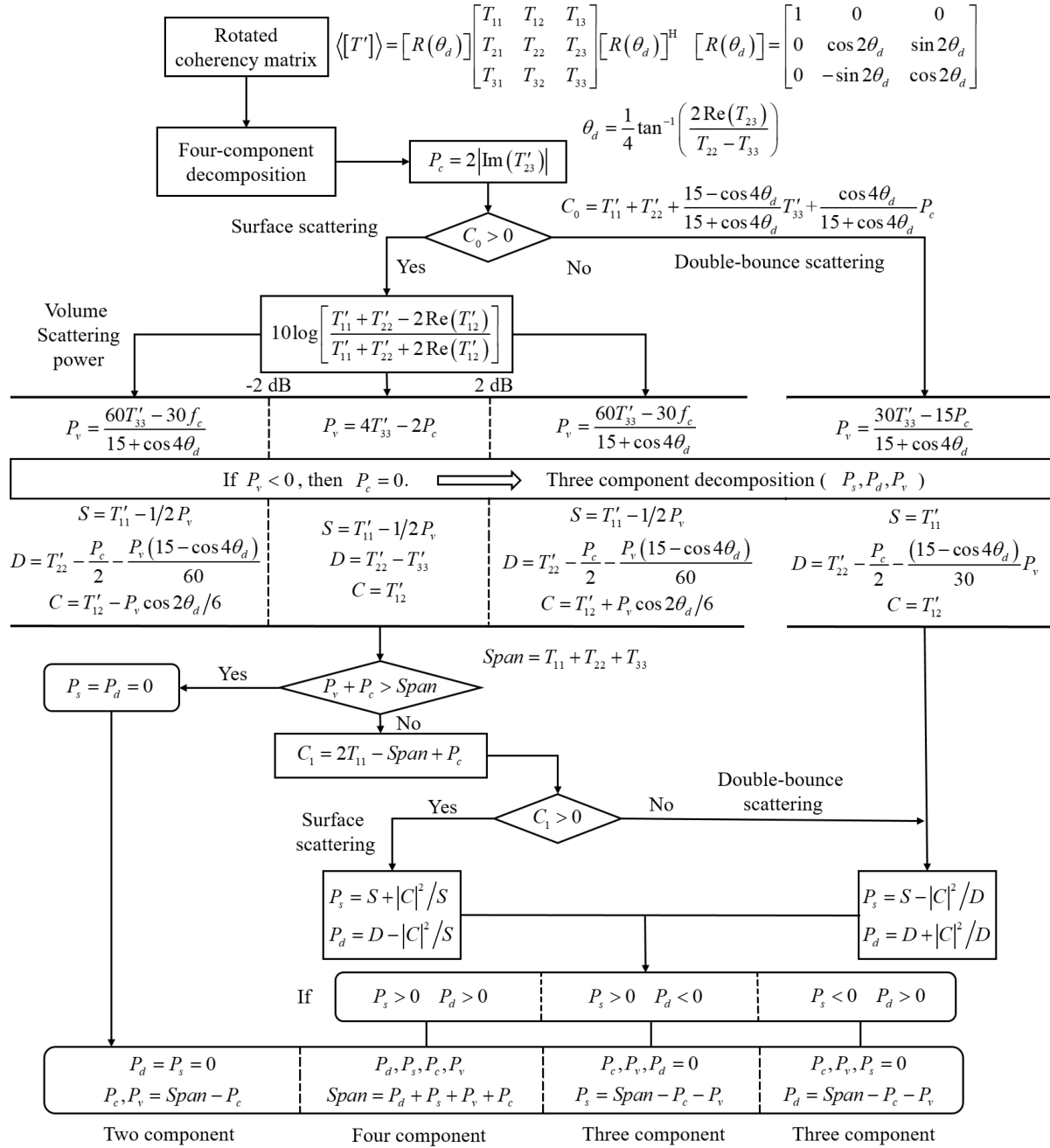Two component   Four component   Three component   Three component

Fig. 1.   Flowchart of the proposed four-component decomposition method.

optical image and the corresponding Pauli pseudo-color map are shown in Fig. 2.

The orange rectangular areas [shown in Fig. 2(b)] are selected to demonstrate the effectiveness of the proposed method. To evaluate the proposed method, the decomposition results are compared with the results obtained via the FDD, FD/GVSM, Y4R, S4R, ExG4URcc, SNVSM, and EE4AVM. The pseudo color images obtained by these eight decomposition methods are shown in Fig. 3. In Fig. 3, compared with the seven existing methods, the entire decomposition results obtained via the proposed method [shown in Fig. 3(h)] seem more "red," which indicates that the double-bounce scattering power obtained via

(a)   (b)

Fig. 2.   Image of the study site in San Francisco, USA. (a) Optical image from Google Earth. (b) Corresponding color-coded Pauli decomposition obtained from the GF-3 dataset with red (double-bounce), green (volume scattering), and blue (surface scattering).
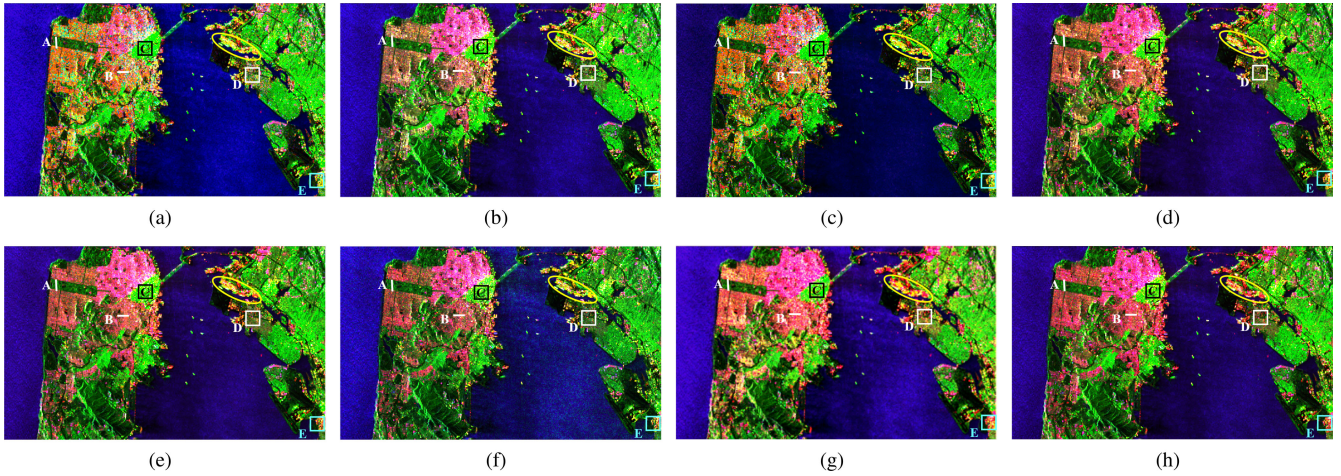
Fig. 3. Decomposition results using different decomposition methods with red (double-bounce scattering), green (volume scattering), and blue (surface scattering). (a) Decomposition map using FDD. (b) Decomposition map using FD/GVSM. (c) Decomposition map using Y4R. (d) Decomposition map using S4R. (e) Decomposition map using ExG4URcc. (f) Decomposition map using SNVSM. (g) Decomposition map using EE4AVM. (h) Decomposition map using ExS4R.
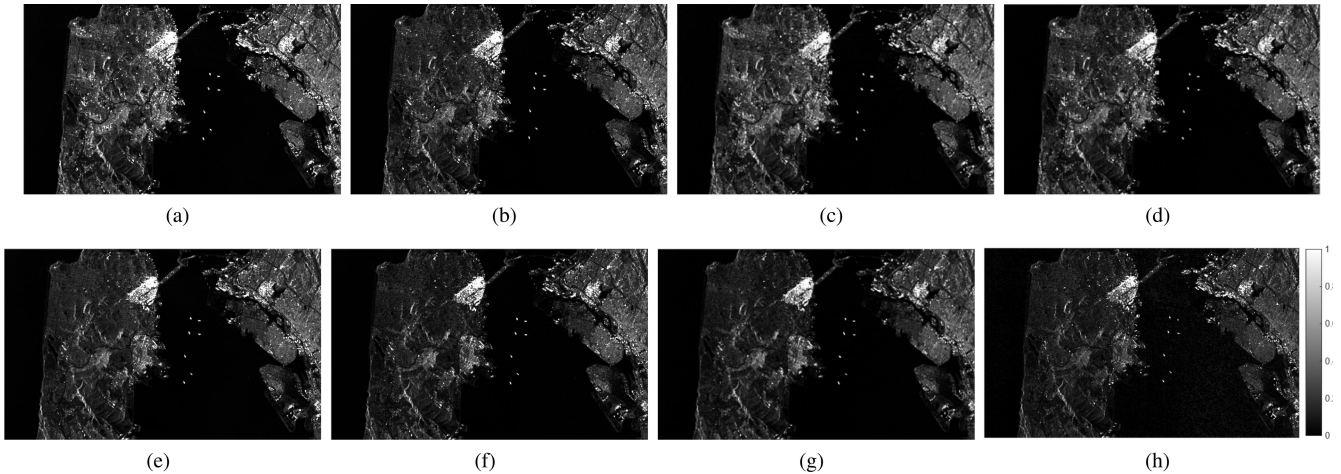

Fig. 4. Magnitude of volume scattering component using different decomposition methods. (a) FDD. (b) FD/GVSM. (c) Y4R. (d) S4R. (e) ExG4URcc. (f) SNVSM. (g) EE4AVM. (h) ExS4R.

the proposed method is stronger than the decomposition results obtained via the existing methods. In addition, it can be seen from the volume scattering images (shown in Fig. 4) obtained via the aforementioned eight methods that the proposed method can effectively reduce the volume scattering powers in the building areas and the OVS can be overcome.

To quantitatively evaluate the performance of the proposed method, the scattering power contributions of the images shown in Fig. 3 are listed in Table I. In Table I, compared with the existing seven decomposition methods, the volume scattering contribution obtained via ExS4R decreases for the whole image and the double-bounce scattering increases properly.

The same conclusions can be more easily drawn by analyzing the plots along the cuts. Two small cuts (25 pixels) in the white lines in Fig. 3 were used to illustrate the profiles of scattering characteristics over forest (cut A) and orthogonal building areas (cut B). In Fig. 5(a) and (b), all methods have similar trends for most pixels of the forest cut. The double-bounce scattering

TABLE I
SCATTERING POWER CONTRIBUTION (%) OF GF-3 IMAGE

Methods	P_s	P_v	P_d	P_c
FDD	51.71	33.47	14.82	–
FD/GVSM	52.87	29.36	17.77	–
Y4R	51.98	29.42	15.59	3.01
S4R	52.23	28.94	15.82	3.01
ExG4URcc	52.92	26.61	17.46	3.01
SNVSM	53.75	25.28	17.95	3.02
EE4AVM	53.76	25.21	18.04	2.99
ExS4R	53.78	25.15	18.06	3.01

obtained via the SNVSM does not change much along the cut. The volume scattering power obtained via the ExS4R increases as shown in Fig. 5(c). Since the satellite is working in the C-band,
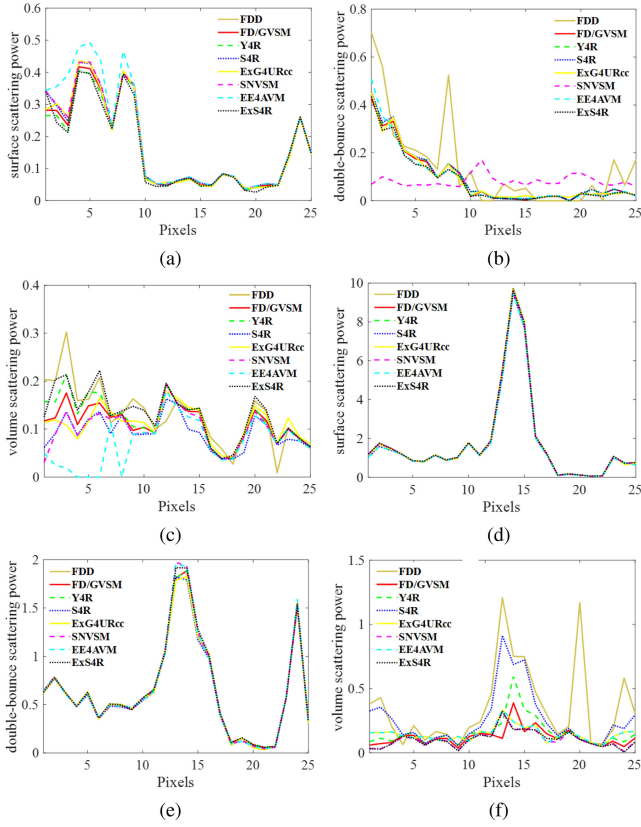
Fig. 5. Power statistics for the selected cuts (cut A and cut B) shown in Fig. 3. (a)–(c) Surface, double-bounce, and volume scattering powers along cut A, respectively. (d)–(f) Surface, double-bounce, and volume scattering powers along cut B, respectively.

Fig. 6. (a)–(c) Enlarged optimal images of the selected study sites "C," "D," and "E," respectively. (d)–(f) Histograms of the orientation angles for the selected study sites "C," "D," and "E," respectively.

Fig. 7. Mean power statistics for the decomposition results obtained via the FDD, FD/GVSM, Y4R, S4R, ExG4URcc, SNVSM, EE4AVM, and ExS4R. (a) Patch "C." (b) Patch "D." (c) Patch "E."

it is hard to penetrate the canopy and the dominant scattering of the forest area is volume scattering. The profiles of the scattering characteristics over forest areas are consistent with the ground truth. In the orthogonal building areas [shown in Fig. 5(d)–(f)], compared with existing methods, the surface and double-bounce scattering powers obtained via the ExS4R increase, while the volume scattering power strength consistently diminishes for almost all the pixels of the cut. Since the dominant terrain types of the orthogonal building areas are buildings and flat ground, the dominant scattering mechanisms are double-bounce and surface scattering. Therefore, the decomposition results are supported by ground reference and the OVS is appropriately overcome, accordingly, using the proposed method. Experimental results show that the proposed method has advantages in analyzing the scattering characteristics of the forests and orthogonal building areas.

B. Quantitative Evaluation of Decomposition Results

To quantitatively evaluate the performance of the previously described decomposition methods (FDD, FD/GVSM, Y4R, S4R, ExG4URcc, SNVSM, EE4AVM, and ExS4R), three oriented building areas (patches "C," "D," and "E") marked with black, white, and cyan rectangles in Fig. 3, respectively, are used to analyze the contribution of various scattering powers. The enlarged optical images of these selected patches are shown
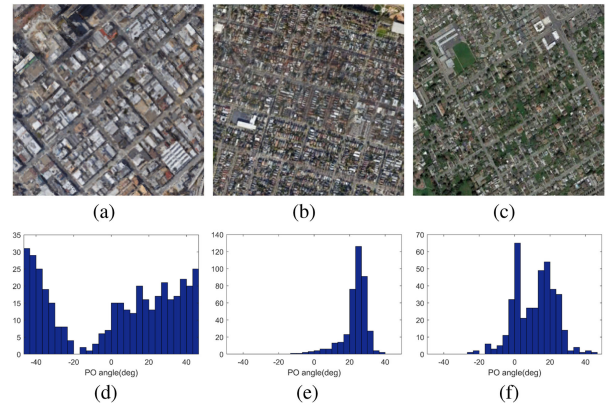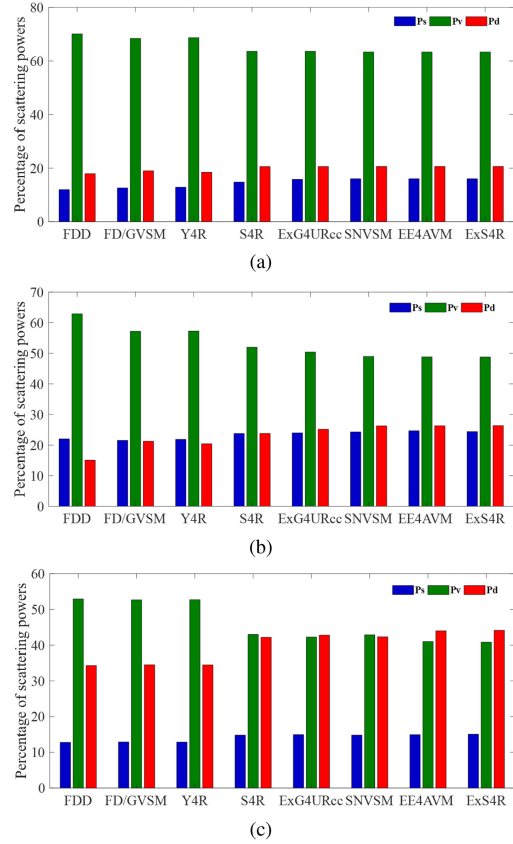
in Fig. 6(a)–(c), respectively, and the corresponding orientation angles of these three patches are shown in Fig. 6(d)–(f), respectively. According to Fig. 6(d)–(f), it is clear that the distribution of the orientation angles differ from each other. The mean power statistics of each patch are shown in the form of histograms in Fig. 7, and the averaged scattering powers of each patch are listed in Tables II–IV.

TABLE II
AVERAGE SCATTERING POWERS (AREA "C")

Methods	P_s	P_v	P_d	P_c
FDD	0.3120	0.9378	0.3047	–
FD/GVSM	0.3201	0.9207	0.3255	–
Y4R	0.3246	0.9211	0.3389	0.1041
S4R	0.3275	0.8850	0.3721	0.1041
ExG4URcc	0.3396	0.8403	0.3974	0.1040
SNVSM	0.3420	0.8371	0.4052	0.1041
EE4AVM	0.3451	0.8359	0.4053	0.1040
ExS4R	0.3424	0.8371	0.4051	0.1041

TABLE IV
AVERAGE SCATTERING POWERS (AREA "E")

Methods	P_s	P_v	P_d	P_c
FDD	0.3120	0.7378	0.5047	–
FD/GVSM	0.3195	0.6988	0.6004	–
Y4R	0.3214	0.6975	0.6008	0.0994
S4R	0.3222	0.6484	0.6491	0.0994
ExG4URcc	0.3207	0.6490	0.6259	0.0994
SNVSM	0.3292	0.6416	0.6471	0.0994
EE4AVM	0.3311	0.6387	0.6480	0.0994
ExS4R	0.3324	0.6371	0.6502	0.0994

TABLE III
AVERAGE SCATTERING POWERS (AREA "D")

Methods	P_s	P_v	P_d	P_c
FDD	0.4102	0.4671	0.4015	–
FD/GVSM	0.4231	0.4479	0.4247	–
Y4R	0.4224	0.4403	0.4240	0.1113
S4R	0.4235	0.4371	0.4261	0.1113
ExG4URcc	0.4305	0.4274	0.4486	0.1113
SNVSM	0.4394	0.4211	0.4573	0.1113
EE4AVM	0.4466	0.4207	0.4574	0.1113
ExS4R	0.4471	0.4212	0.4577	0.1113

In the patch "C," the buildings are oriented at a large angle to the direction of radar line of sight. After the OAC operation, the buildings in patch "C" are appropriately $10°$–$20°$ oriented away from the radar line of sight. The residual orientation angle affects the final decomposition accuracy. In Fig. 7(a), compared with the decomposition results obtained by the FDD, FD/GVSM, Y4R, S4R, ExG4URcc, SNVSM, and EE4AVM, the percentage of surface scattering power obtained by the ExS4R is increased by 4.04%, 3.44%, 3.18%, 0.23%, 0.25%, 0.03%, and 0.02%, respectively, and the percentage of double-bounce scattering power obtained by the ExS4R is increased by 2.73%, 1.64%, 2.18%, 0.04%, 0.03%, 0.02%, and 0.003%, respectively. In the proposed method, the contributions of the double-bounce and surface scattering powers of the oriented buildings in the area "C" are properly enhanced, and the flat ground between the buildings can be correctly decomposed into surface scattering. Therefore, the ExS4R can be used to characterize the scattering mechanism of the building areas with large orientation angles, and the decomposition results shown in Fig. 3(h) demonstrate that the dominant scattering of this area can be reasonably interpreted.

According to Fig. 7(b) and Table III, for the oriented area "D," the volume scattering power obtained via ExS4R obviously decreases and the reduced scattering powers are transformed into the surface scattering and double-bounce scattering components. Compared with the contribution statistics obtained via the FDD, FD/GVSM, Y4R, S4R, ExG4URcc, SNVSM, and EE4AVM, the percentage of double-bounce scattering power obtained by the ExS4R is increased by 11.32%, 5.14%, 5.94%, 2.59%, 1.21%, 0.11%, and 0.09%, respectively, and the percentage of volume

scattering power obtained by the ExS4R is decreased by 14.13%, 8.43%, 8.48%, 3.21%, 1.64%, 0.22%, and 0.05%, respectively. According to the optical image shown in Fig. 6(b), the dominant scattering mechanisms of the study site are the double-bounce scattering and surface scattering, and the proposed method can obtain decomposition results which are supported by ground reference.

For the oriented building area "E," the orientation angles of the buildings are small and the contribution of double-bounce scattering is high. According to Fig. 7(c), compared with the contribution statistics obtained by the FDD, FD/GVSM, Y4R, S4R, ExG4URcc, SNVSM, and EE4AVM, the percentage of double-bounce scattering power obtained by the ExS4R is increased by 9.84%, 9.65%, 9.68%, 1.94%, 1.34%, 1.81%, and 0.15%, respectively, and the percentage of volume scattering power obtained by the ExS4R is decreased by 12.11%, 11.81%, 11.86%, 0.17%, 1.44%, 2.05%, and 0.17%, respectively. The volume scattering power can be reduced and the OVS can be overcome.

Experimental results of the selected patches demonstrate that the proposed method can successfully discriminate the cross-pol component from the entire HV component to obtain reasonable decomposition results, which are consistent with the actual land covers. Although the decomposition results obtained via ExG4URcc, SNVSM, EE4AVM, and ExS4R have similar performance in the building areas, the computational efficiency of the proposed method is better than the other three methods. This phenomenon can be explained as follows: In the ExG4URcc, the ratio of correlation coefficient (Rcc) must be adopted to substitute the refined branch condition for its sensibility of scattering characteristics and the threshold should be analyzed at first, which requires additional analysis. In the SNVSM, the optimal method is employed to determine the parameters, which is limited by the computational efficiency due to the additional calculation load. As for EE4AVM, the LUT must be applied to link the eigen-decomposition and model-based decomposition, which requires more calculations. Therefore, in terms of computational efficiency and accuracy, the ExS4R is an appropriate approach.

To further evaluate the performance of the proposed approach, the red transect in Fig. 2(b) is used to analyze the potential of the volume scattering powers using various decomposition methods. The transect includes parks, orthogonal buildings, and oriented buildings, and the distribution of the area is shown in
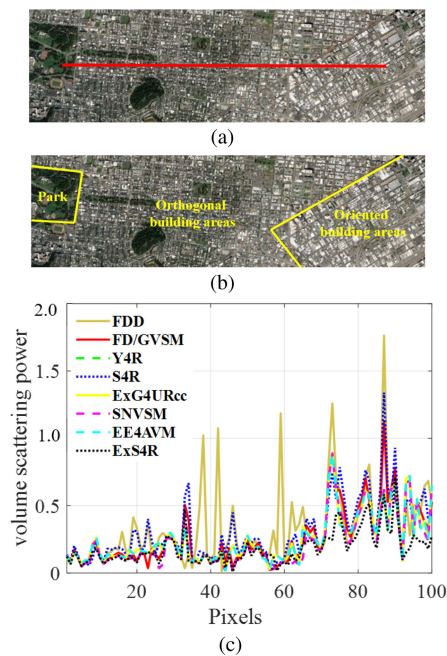
Fig. 8. Image of the red transect shown in Fig. 2(b). (a) Photograph by Google Earth. (b) Map of this test area. (c) Volume scattering power profiles of eight decomposition methods.

Fig. 8(a) and (b). The volume scattering power obtained via the considered decomposition methods along the transect direction is shown in Fig. 8(c). In the volume scattering statistics along the transect direction, the volume scattering powers obtained by these eight decomposition methods have similar trends in various terrain types. From Fig. 8(c), it is found that, compared with the seven existing decomposition methods, the volume scattering obtained by the proposed method is very low in orthogonal and oriented building areas and has a similar trend in the forest areas. Therefore, it is possible to reasonably retain the volume scattering powers while overcoming the OVS, accordingly, using the proposed method.

In the entire image, the area with a large number of containers can also be used to evaluate the performance of these decomposition methods (yellow ellipses shown in Fig. 3). The containers exhibit the same scattering characteristics as the building areas and the dominant scattering mechanism is double-bounce scattering or surface scattering. In the decomposition results shown in Fig. 3, the FDD, FD/GVSM, Y4R, and SNVSM cannot correctly represent the scattering characteristics of the containers in this area, and the scattering characteristics of a small number of containers can be interpreted using the S4R, ExG4URcc, and EE4AVM. According to Fig. 3(h), the scattering characteristics of this area can be reasonably interpreted using the proposed decomposition method. In the ExS4R, the dominant scattering mechanism of the containers is double-bounce scattering, and surface scattering occurs in the flat ground areas between containers.

For model-based decomposition method, the occurrence of negative scattering powers is an important indicator to evaluate the performance of the method. Negative scattering powers

typically occur in surface scattering or double-bounce scattering because of the prioritized calculation of the volume and helix scattering components. The percentage of the negative scattering powers obtained via the aforementioned six decomposition methods are listed in Table V. It can be seen that, compared with the five existing decomposition methods, the percentage of negative scattering powers of the proposed method is reduced by 7.7%, 6.0%, 6.4%, 1.5%, 1.1%, 0.1%, and 0.3%, respectively. Thus, the proposed method has the potential to reduce the negative scattering powers.

C. Experiments on the E-SAR L-Band Data

To provide further verification of the new decomposition scheme, the proposed method is also applied to other fully Pol-SAR images in terms of different frequency and resolution. The E-SAR L-band fully polarized SAR data with a spatial resolution of 1.5×1.8 m (range $\times$ azimuth) acquired over Oberpfaffen-hofen, Germany, are used for experiments. The study site is 1300×1200 pixels in size. The incidence angle is about $40°$, and the central coordinates of the study site are $(48°5'3,'' 11°17'4'')$. As the equivalent number of looks of the data is high enough, no more averaging or filter is needed. The optical image corresponding to the data is shown in Fig. 9(a) and the decomposition results corresponding to the FDD, FD/GVSM, Y4R, S4R, ExG4URcc, SNVSM, EE4AVM, and ExS4R are shown in Fig. 9(b)–(i), respectively.

Two study sites of the image (labeled "A" and "B" in Fig. 9) are selected to further analyze the differences of the decomposition results. The enlarged RGB composition images of two selected study sites are shown in Figs. 10 and 11, respectively. In Fig. 10, with the extension of the decomposition method, the green building blocks in the middle of the FDD decomposition results [shown in Fig. 10(a)] mostly become cyan in the ExG4URcc decomposition results [shown in Fig. 10(e)], and this cyan site becomes stronger and brighter in the SNVSM, EE4AVM, and ExS4R decomposition images [shown in Fig. 10(f)–(h), respectively], which means that the volume scattering components are reduced in the SNVSM, EE4AVM, and ExS4R. The SNVSM, EE4AVM, and ExS4R decomposition results of the oriented buildings in study site "A" have similar performance. In addition, the highway marked via red ellipse in Fig. 10 turns into a mix of blue and magenta in the ExS4R decomposition image [shown in Fig. 10(h)], which means that the double-bounce scattering and surface scattering strength remarkably increase in the ExS4R. Since the double-bounce scattering caused by ground-highway interaction mostly dominates for the backscatters of highway, the decomposition results of the ExS4R better reveal the scattering characteristic of the targets. According to Fig. 11, the scattering mechanisms of study site "B" cannot be reasonably interpreted using the existing decomposition methods and the dominant scattering mechanism of many oriented buildings is mis-decomposed into volume scattering, leading to the OVS. Compared with the results obtained via the existing decomposition methods [shown in Fig. 11(a)–(g)], the profiles of the oriented buildings obtained via the ExS4R [shown in Fig. 11(h)] are much clear and mainly shown in red or magenta.

TABLE V
PERCENTAGE OF PIXELS WITH NEGATIVE SCATTERING POWERS (%)

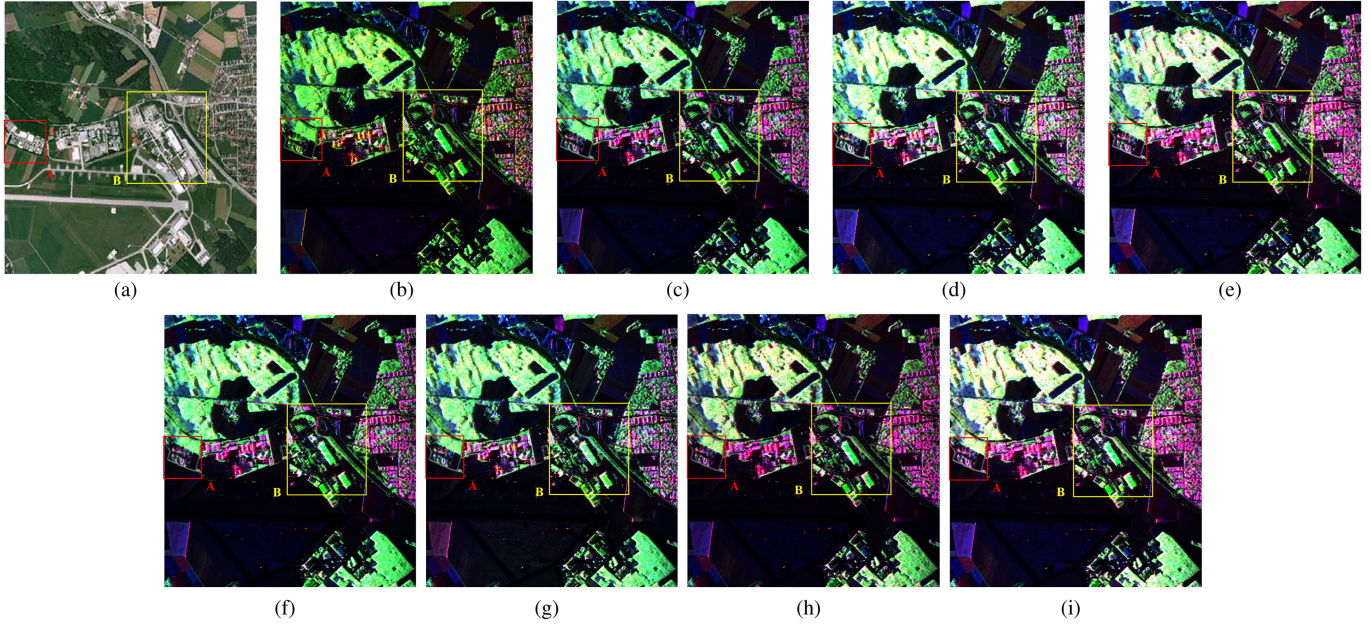| Methods	FDD	FD/GVSM	Y4R	S4R	ExG4URcc	SNVSM	EE4AVM	ExS4R
Percentage of negative scattering powers (%)	27.4	25.7	26.1	21.2	20.8	19.8	20.0	19.7

Fig. 9. Image of the study site in Oberpfaffenhofen, Germany. (a) Optical image of the study site. (b) Decomposition map using FDD. (c) Decomposition map using FD/GVSM. (d) Decomposition map using Y4R. (e) Decomposition map using S4R. (f) Decomposition map using ExG4URcc. (g) Decomposition map using SNVSM. (h) Decomposition map using EE4AVM. (i) Decomposition map using ExS4R. Red (double-bounce scattering), green (volume scattering), and blue (surface scattering).
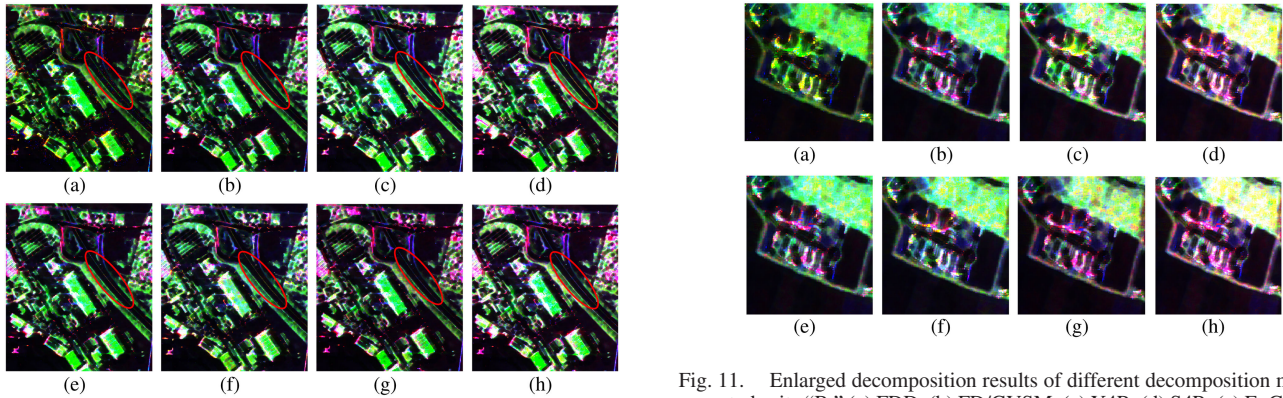

Fig. 10. Enlarged decomposition results of different decomposition methods over study site "A." (a) FDD. (b) FD/GVSM. (c) Y4R. (d) S4R. (e) ExG4URcc. (f) SNVSM. (g) EE4AVM. (h) ExS4R.

Fig. 11. Enlarged decomposition results of different decomposition methods over study site "B." (a) FDD. (b) FD/GVSM. (c) Y4R. (d) S4R. (e) ExG4URcc. (f) SNVSM. (g) EE4AVM. (h) ExS4R.

Since the dominant scattering components of the oriented buildings are surface scattering and double-bounce scattering, the scattering mechanisms obtained by the ExS4R are supported by ground reference. The volume scattering of the oriented building areas can be reduced via the ExS4R and the OVS can be overcome.

The scattering power contribution in these two selected study sites are listed in Table VI. It can be seen from the table that, compared with the FDD, FD/GVSM, Y4R, S4R, ExG4URcc, SNVSM, and EE4AVM, the contributions of the double-bounce scattering and surface scattering increase in the ExS4R. This denotes that, by using the ExS4R, volume scattering power can be reasonably reduced and more building areas can be identified without OVS.

As a result, in terms of the accuracy of the decomposition results, the percentage of negative scattering powers, and the calculation load, the proposed method is a satisfactory decomposition approach.

TABLE VI
SCATTERING POWER CONTRIBUTION OF THE SELECTED STUDY SITES (%).

| Method	A			B		
	P_s	P_v	P_d	P_s	P_v	P_d
FDD	41.46	37.48	21.06	43.62	37.21	19.17
FD/GVSM	41.85	35.14	23.01	43.78	33.07	23.15
Y4R	41.87	35.17	22.94	44.39	33.38	22.21
S4R	50.09	26.90	22.99	54.04	21.47	24.47
ExG4URcc	50.06	26.92	23.00	54.27	21.31	24.40
SNVSM	50.13	26.67	23.17	54.31	21.29	24.37
EE4AVM	50.18	26.62	23.18	54.40	20.97	24.61
ExS4R	**50.16**	**26.61**	**23.21**	**54.51**	**20.46**	**25.01**

IV. CONCLUSION

In this article, a modified four-component decomposition method for PolSAR image processing is proposed. By placing the orientation angles in the probability density models, general forms of the volume scattering models and branch conditions can be obtained. Since the orientation angles are contained in the volume scattering models, this new decomposition method can be used for various landscapes with different orientation angles, and the decomposition results are supported by ground reference. The scattering mechanisms of oriented buildings can be discriminated from the vegetation areas and the OVS can be substantially overcome. It is noted that, under certain conditions, the general forms of the volume scattering models and branch conditions are consistent with the results obtained by the S4R. In this article, GF-3 data and E-SAR data are used to demonstrate the effectiveness of the proposed method. The experimental results show that the proposed method can discriminate the oriented buildings from the vegetation areas and the reasonable scattering mechanisms of various terrain types can be obtained. At the same time, the vegetation areas and the orthogonal building areas can be decomposed correctly. With the refined volume estimation models, the proposed method, which overcomes the OVS and the ambiguity of the scattering mechanisms in urban areas, is proved as a satisfactory decomposition approach.

REFERENCES

[1] L. Deng and C. Wang, "Improved building extraction with integrated decomposition of time-frequency and entropy-alpha using polarimetric SAR data," *IEEE J. Sel. Topics Appl. Earth Observ. Remote Sens.*, vol. 7, no. 10, pp. 4058–4068, Oct. 2014.

[2] D. Xiang, T. Tang, J. Ban, Y. Su, and G. Kuang, "Unsupervised polarimetric SAR urban area classification based on model-based decomposition with cross scattering," *ISPRS J. Photogrammetry Remote Sens.*, vol. 116, pp. 86–100, 2016.

[3] Y. Xi, H. Lang, Y. Tao, L. Huang, and Z. Pei, "Four-component model-based decomposition for ship targets using PolSAR data," *Remote Sens.*, vol. 9, no. 6, pp. 621–638, 2016.

[4] Y. Hu, J. Fan, and J. Wang, "Classification of PolSAR images based on adaptive nonlocal stacked sparse autoencoder," *IEEE Geosci. Remote Sens. Lett.*, vol. 15, no. 7, pp. 1050–1054, Jul. 2018.

[5] J. R. Huynen, "Measurement of the target scattering matrix," *Proc. IEEE*, vol. 53, no. 8, pp. 936–946, Aug. 1965.

[6] J. R. Huynen, "Phenomenological theory of radar targets," *Electromagn. Scattering*, pp. 653–712, 1978.

[7] J. R. Huynen, "The stokes matrix parameters and their interpretation in terms of physical target properties," *Proc. SPIE*, vol. 1317, pp. 195–207, 1990.

[8] G. M. Vachula and R. M. Barnes, "Polarization detection of a fluctuating radar target," *IEEE Trans. Aerosp. Electron. Syst.*, vol. AES-19, no. 2, pp. 250–257, Mar. 1983.

[9] S. R. Cloude, "Target decomposition theorems in radar scattering," *Electron. Lett.*, vol. 21, no. 1, pp. 22–24, 1985.

[10] J. J. van Zyl, "Unsupervised classification of scattering behavior using radar polarimetry data," *IEEE Trans. Geosci. Remote Sens.*, vol. 27, no. 1, pp. 36–45, Jan. 1989.

[11] A. Freeman, "SAR calibration: An overview," *IEEE Trans. Geosci. Remote Sens.*, vol. 30, no. 6, pp. 1107–1122, Nov. 1992.

[12] J. S. Lee, M. R. Grunes, and R. Kwok, "Classification of multi-look polarimetric SAR imagery based on complex Wishart distribution," *Int. J. Remote Sens.*, vol. 15, no. 11, pp. 2299–2311, 1994.

[13] R. Touzi and A. Lopes, "Statistics of the stokes parameters and of the complex coherence parameters in one-look and multi-look speckle fields," *IEEE Trans. Geosci. Remote Sens.*, vol. 34, no. 2, pp. 519–531, Mar. 1996.

[14] J. S. Lee, M. R. Grunes, T. L. Ainsworth, L. J. Du, D. L. Schuler, and S. R. Cloude, "Unsupervised classification using polarimetric decomposition and the complex Wishart classifier," *IEEE Trans. Geosci. Remote Sens.*, vol. 37, no. 5, pp. 2249–2258, Sep. 1999.

[15] S. R. Cloude and E. Pottier, "A review of target decomposition theorems in radar polarimetry," *IEEE Trans. Geosci. Remote Sens.*, vol. 34, no. 2, pp. 498–518, Mar. 1996.

[16] A. Freeman and S. L. Durden, "A three-component scattering model for polarimetric SAR data," *IEEE Trans. Geosci. Remote Sens.*, vol. 36, no. 3, pp. 963–973, May 1998.

[17] Y. Yamaguchi, T. Moriyama, M. Ishido, and H. Yamada, "Four-component scattering model for polarimetric SAR image decomposition," *IEEE Trans. Geosci. Remote Sens.*, vol. 43, no. 8, pp. 1699–1706, Aug. 2005.

[18] Y. Yamaguchi, A. Sato, W. M. Boerner, R. Sato, and H. Yamada, "Four-component scattering power decomposition with rotation of coherency matrix," *IEEE Trans. Geosci. Remote Sens.*, vol. 49, no. 6, pp. 2251–2258, Jun. 2011.

[19] O. Antropov, Y. Rauste, and T. Hame, "Volume scattering modeling in PolSAR decompositions: Study of ALOS PALSAR data over boreal forest," *IEEE Trans. Geosci. Remote Sens.*, vol. 49, no. 10, pp. 3838–3848, Oct. 2011.

[20] A. Sato, Y. Yamaguchi, G. Singh, and S. Park, "Four-component scattering power decomposition with extended volume scattering model," *IEEE Geosci. Remote Sens. Lett.*, vol. 9, no. 2, pp. 166–170, Mar. 2012.

[21] S. Chen, X. Wang, Y. Li, and M. Sato, "Adaptive model-based polarimetric decomposition using POLinSAR coherence," *IEEE Trans. Geosci. Remote Sens.*, vol. 52, no. 1, pp. 1705–1718, Mar. 2014.

[22] Q. Xie, J. Zhu, J. M. Lopez-Sanchez, C. Wang, and H. Fu, "A modified general polarimetric model-based decomposition method with the simplified Neumann volume scattering model," *IEEE Geosci. Remote Sens. Lett.*, vol. 15, no. 8, pp. 1229–1233, Aug. 2018.

[23] S. Cloude and E. Pottier, "An entropy based classification scheme for land applications of polarimetric SARs," *IEEE Trans. Geosci. Remote Sens.*, vol. 35, no. 1, pp. 68–78, Jan. 1997.

[24] C. Wang, W. Yu, R. Wang, Y. Deng, and F. Zhao, "Comparison of nonnegative eigenvalue decompositions with and without reflection symmetry assumptions," *IEEE Trans. Geosci. Remote Sens.*, vol. 52, no. 4, pp. 2278–2287, Apr. 2014.

[25] F. Zhu, Y. Zhang, and L. Dong, "Eigenvalue/eigenvector-based serial decomposition of the polarimetric synthetic aperture radar coherency matrix," *IET Radar Sonar Navig.*, vol. 12, no. 2, pp. 209–217, 2018.

[26] G. Singh, Y. Yamaguchi, and S. E. Park, "General four-component scattering power decomposition with unitary transformation of coherency matrix," *IEEE Trans. Geosci. Remote Sens.*, vol. 51, no. 5, pp. 3014–3022, Feb. 2013.

[27] A. Bhattacharya, G. Singh, S. Manickam, and Y. Yamaguchi, "An adaptive general four-component scattering power decomposition with unitary transformation of coherency matrix (AG4U)," *IEEE Geosci. Remote Sens. Lett.*, vol. 12, no. 10, pp. 2110–2114, Oct. 2015.

[28] S. Quan, D. Xiang, B. Xiong, H. Canbin, and K. Gangyao, "A hierarchical extension of general four-component scattering power decomposition," *Remote Sens.*, vol. 9, no. 8, 2017, Art. no. 856.

[29] Q. Xie, J. Ballester-Berman, J. Lopez-Sanchez, J. Zhu, and C. Wang, "On the use of generalized volume scattering models for the improvement of general polarimetric model-based decomposition," *Remote Sens.*, vol. 9, no. 2, 2017, Art. no. 117.

[30] D. Ratha, D. Mandal, V. Kumar, H. McNairn, A. Bhattacharya, and A. C. Frery, "A generalized volume scattering model-based vegetation index from polarimetric SAR data," *IEEE Geosci. Remote Sens. Lett.*, vol. 16, no. 11, pp. 1791–1795, Nov. 2019.

[31] S. Zhang *et al.*, "Multiple-component scattering model for polarimetric SAR image decomposition," *IEEE Geosci. Remote Sens. Lett.*, vol. 5, no. 4, pp. 603–607, Oct. 2008.

[32] D. Xiang, W. Wei, T. Tao, and Y. Su, "Multiple-component polarimetric decomposition with new volume scattering models for PolSAR urban areas," *IET Radar Sonar Navig.*, vol. 11, no. 3, pp. 410–419, 2017.

[33] Y. Wang, W. Yu, X. Liu, and C. Wang, "A hierarchical extended multiple-component scattering decomposition of polarimetric SAR interferometry," *IEEE Geosci. Remote Sens. Lett., 2020,* to be published, doi: 10.1109/LGRS.2019.2942090.

[34] Q. Xie, J. Ballester-Berman, J. Lopez-Sanchez, J. Zhu, and C. Wang, "Quantitative analysis of polarimetric model-based decomposition methods," *Remote Sens.*, vol. 8, no. 12, 2016, Art. no. 977.

[35] B. Zou, D. Lu, L. Zhang, and W. M. Moon, "Eigen-decomposition-based four-component decomposition for PolSAR data," *IEEE J. Sel. Topics Appl. Earth Observ. Remote Sens.*, vol. 9, no. 3, pp. 1286–1296, Mar. 2016.

[36] S. W. Chen, M. Ohki, M. Shimada, and M. Sato, "Deorientation effect investigation for model-based decomposition over oriented built-up areas," *IEEE Geosci. Remote Sens. Lett.*, vol. 10, no. 2, pp. 273–277, Mar. 2013.

[37] X. Sun, H. Song, R. Wang, and L. Ning, "High-resolution polarimetric SAR image decomposition of urban areas based on a POA correction method," *Remote Sens. Lett.*, vol. 9, no. 4, pp. 363–372, 2018.

[38] Y. Cui, Y. Yamaguchi, J. Yang, H. Kobayashi, S. Park, and G. Singh, "On complete model-based decomposition of polarimetric SAR coherency matrix data," *IEEE Trans. Geosci. Remote Sens.*, vol. 52, no. 4, pp. 1991–2001, Apr. 2014.
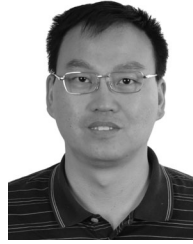
Weidong Yu (Member, IEEE) was born in Henan, China, in 1969. He received the M.Sc. and Ph.D. degrees in electrical engineering from the Nanjing University of Aeronautics and Aerospace, Nanjing, China, in 1994 and 1997, respectively.

He has been with the Institute of Electronic, Chinese Academy of Science (IECAS) since 1997, and became a Professor of communication and information systems, in 2000. His current research interests include airborne and spaceborne SAR system design and their signal processing. He has authored more than 50 papers and holds five patents. He has been the Chief Designer for several SAR systems and is currently the Deputy Director with the Department of Space Microwave Remote Sensing System, IECAS.

Chunle Wang received the B.S. degree in electronic information engineering from the Beijing Information Science and Technology University, Beijing, China, in 2008. She received the Ph.D. degree in image classification and polarimetric target decomposition technique for polarimetric synthetic aperture radar from Institute of Electronics, Chinese Academy of Sciences, Beijing, China, in 2013.

Currently, she is an Associate Research Assistant of SAR system design and their image processing with Institute of Electronic, Chinese Academy of Sciences, Beijing, China. Her current research interests include classification and polarimetric target decomposition technique for polarimetric synthetic aperture radar in the University of Chinese Academy of Sciences, Beijing, China.
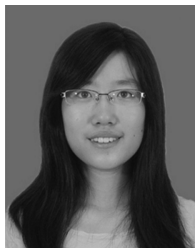
Yu Wang (Student Member, IEEE) born in Shandong, China, in 1993. She received the B.S. degree in telecommunication engineering from Jilin University, Jilin, China, in 2016. She is currently pursuing the Ph.D. degree in image classification and target decomposition technique for polarimetric synthetic aperture radar and polarimetric interferometric synthetic aperture radar with the University of Chinese Academy of Science, Beijing, China.

Xiuqing Liu graduated in polarimetric and polarimetric information processing from the Institute of Electronics, Chinese Academy of Sciences, Beijing, China, in 2004.

She is currently an Associate Researcher with the Institute of Aerospace Information Innovation of the Chinese Academy of Sciences. Her main research directions are polarimetric/compact polarimetric SAR system technology, polarimetric/compact polarimetric SAR data processing, and information extraction.